*To be published in Optics Letters:*

**Title:** Perfectly vertical surface grating couplers using subwavelength engineering for increased feature sizes

**Authors:** Mohsen Kamandar Dezfouli,Yuri Grinberg,Daniele Melati,Pavel Cheben,Jens Schmid,Alejandro Sánchez-Postigo,Alejandro Ortega-Moñux,J. Gonzalo Wangüemert-Pérez,Ross Cheriton,Siegfried Janz,Dan-Xia Xu

**Accepted:** 18 May 20

**Posted** 18 May 20

**DOI:** https://doi.org/10.1364/OL.395292

# Perfectly vertical surface grating couplers using subwavelength engineering for increased feature sizes

MOHSEN KAMANDAR DEZFOULI[1], YURI GRINBERG[2], DANIELE MELATI[1], PAVEL CHEBEN[1], JENS H. SCHMID[1], ALEJANDRO SÁNCHEZ-POSTIGO[3], ALEJANDRO ORTEGA-MOÑUX[3], GONZALO WANGÜEMERT-PÉREZ[3], ROSS CHERITON[1], SIEGFRIED JANZ[1], AND DAN-XIA XU[1]

[1] *Advanced Electronics and Photonics Research Centre, National Research Council Canada, Ottawa, ON K1A 0R6, Canada*
[2] *Digital Technologies Research Centre, National Research Council Canada, Ottawa, ON K1A 0R6, Canada*
[3] *Dpto. de Ingeniería Comunicaciones, ETSI Telecomunicación, Universidad de Málaga, 29010 Málaga, Spain*

*Compiled May 15, 2020*

**We present perfectly vertical grating couplers for the 220 nm SOI platform incorporating subwavelength metamaterials to increase the minimum feature sizes and achieve broadband low back-reflection. Our study reveals devices with high coupling efficiencies are distributed over a wide region of the design space with varied back-reflections, while still maintaining minimum feature sizes larger than 100 nm and even 130 nm. Using 3D-FDTD simulations, we demonstrate devices with broadband low back-reflection of less than -20 dB over more than 100 nm bandwidth centered around the C-band. A coupling efficiency of 72% and 67% are achieved for a minimum feature size of 106 nm and 130 nm, respectively. These gratings are also more fabrication tolerant compared to similar designs not using metamaterials.**



http://dx.doi.org/10.1364/ao.XX.XXXXXX



Integrated silicon photonics has greatly impacted a wide range of scientific and technological advances from optical communication to sensing. Coupling light in and out of these integrated photonic chips not only must be done efficiently, but also allow ease of packaging and circuit-level design flexibility. Surface grating couplers are great solutions to these challenges and therefore they have been widely pursued for improved performance [1–9]. In particular, perfectly vertical grating couplers are appealing as they facilitate coupling light to lasers, detector arrays, and multi-core fibers for space division multiplexing in a straightforward manner.

The design of perfectly vertical grating couplers is fundamentally complicated by the fact that the second order diffraction from the grating reflects back into the input waveguide. Recently, a five-segment design consisting of a pillar and an L-shaped segment was optimized using particle swarm algorithm to arrive at a highly efficient vertical grating coupler with low back-reflection [7]. Using machine learning pattern recognition, our analysis has rigorously shown that the minimum feature size (mFS) for this coupler geometry can never be larger than 88 nm [10]. Such small features are difficult to fabricate with good fidelity and are susceptible to fluctuations in the fabrication process. More recently, inverse design algorithms were applied to the vertical grating coupler problem but relying on either non-trivial geometries or small mFS that might be again difficult to fabricate [9, 11]. For broad adoption in practical applications, fabrication compatibility with deep-UV (DUV) lithography is desirable. Current open-access foundries for 200 mm SOI wafers can in principle accept 100 nm critical dimension, but the design rules for multi-project-wafer (MPW) runs are set at 130 nm [12]. Foundries for 300 mm wafers with immersion DUV lithography can pattern 50 nm features. However these technology nodes are more expensive and not yet open-access. Tong et al. [13] have proposed a vertical grating coupler compatible with DUV lithography with a vertical coupling efficiency (CE) of approximately 63% (experimentally 54%), using a poly-silicon overlayer that adds fabrication complexity.

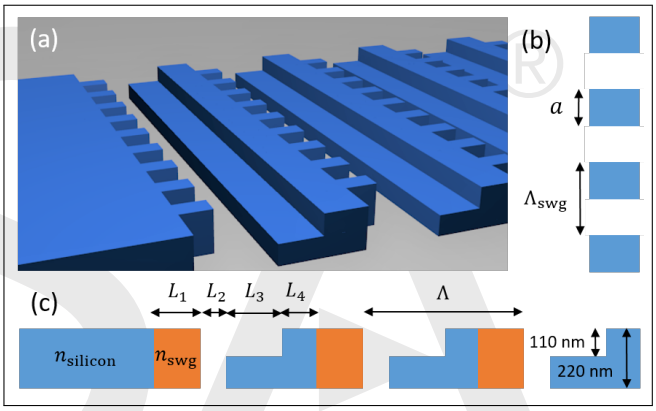


**Fig. 1.** (a) Schematic of the four-segment vertical grating coupler using subwavelength metamaterials. (b) Top view of the SWG segment with a period $\Lambda_{swg}$ and duty cycle $DC_{swg} = a/\Lambda_{swg}$. (c) 2D representation of the device with diffracting period $\Lambda$ and optimization variables $[L_1, L_2, L_3, L_4, n_{swg}]$.

In this work, we present perfectly vertical grating couplers using the commonly available two-step etch configuration on a

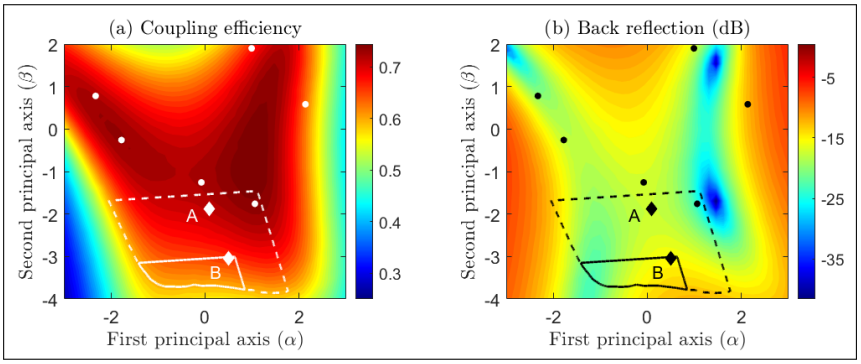


**Fig. 2.** The subspace map for (a) vertical coupling efficiency and (b) back reflection, obtained using the machine learning dimensionality reduction performed on a collection of six good performing devices (marked by dots on the maps). The contours represent the regions where devices with $\geq$ 100 nm (enclosed by the dashed line) and $\geq$ 130 nm (enclosed by the solid line) feature sizes reside. Two devices marked by diamonds are selected for performance comparison and are further optimized using 3D-FDTD.

220 nm silicon-on-insulator (SOI) platform, with a minimum feature size larger than 100 nm. We build on the geometry recently proposed in [10] that incorporates a new subwavelength section into a grating configuration similar to that originally reported in [7]. As schematically shown in Fig. 1(a), each unit-cell is made of four segments, with a section transversely patterned using subwavelength grating (SWG) engineering [14, 15] followed by an L-shaped step that provides the blazing to direct light upwards. This previous work was intended primarily as a validation of our machine learning method for designs involving SWG structures [10]. The results were based on 2D simulation methods and approximations that, while useful for predicting qualitative performance trends, can only give an approximation to full 3D calculations in such geometries [16]. Here, we apply our machine-learning methodology to carry out a more rigorous examination of the design space, and then validate and optimize the best candidates using full 3D-FDTD simulations. Whereas the original SWG design results in Ref. [10] suggested that feature sizes of 100 nm were possible, here we rigorously show that excellent performance can be obtained for devices with minimum feature sizes as large as 130 nm. Furthermore, we achieve an improved low BR of -20 dB over more than 100 nm bandwidth and high CE of 72% at a wavelength of 1550 nm. Slightly compromising the BR to -15 dB, CEs of 75% can be achieved, similar to the best reported results so far [10]. We also highlight the improved fabrication tolerance due to the SWG incorporation, particularly in maintaining the low level of BR.

To implement the machine learning optimization strategy [10], we first optimize our grating structures with 2D-FDTD for better computational efficiency and collect an initial sparse set of good designs. We consider the SWG segment as a homogeneous medium with an effective material index of $n_{\mathrm{swg}}$, as illustrated in Fig. 1(c). The effective index can be related to the pitch and the duty cycle of the SWG segment using either second order effective medium theory or numerical computations [17, 18]. However, we find that the wavelength for the peak CE calculated for our grating geometry in such a manner is blue-shifted by about 40 nm compared to full 3D-FDTD simulations. Additionally the BR spectrum is different between 2D and 3D simulations. This can be attributed to the fact that the effective medium theory holds for simpler geometries, while our SWG geometry is more complex due to the index profile being modulated along the propagation direction. Therefore, we carry out the initial stage of optimization in 2D targeted at the wavelength of $\lambda = 1510$ nm, such that the actual devices verified with 3D-FDTD will be optimized at $\lambda = 1550$ nm. Hence, our design space for 2D simulations can be represented via the set $\mathrm{X} = [L_1, L_2, L_3, L_4, n_{\mathrm{swg}}]$ for the four segment lengths and the SWG index. We consider periodic grating couplers consisting of 25 unit cells. The partial etch-depth is 110 nm (similar to the reports in [7], we have found comparable performances for devices optimized for 70 nm shallow etch, usually with smaller mFS values), the buried oxide layer is 3 µm thick, and the upper oxide cladding is assumed semi-infinite. We design the couplers for a single mode SMF-28 fiber with a modal-field diameter (MFD) of 10.4 µm, located at 2 µm above the grating surface and modeled using a Gaussian profile. In simulations, we excite a 10 µm long input waveguide using its fundamental TE mode and monitor the power reflected back into the same waveguide (at 10 $\mu m$ before the grating starts) as well as the power diffracted upward (at 2 $\mu m$ above the grating) to quantify the device CE and BR, using mode expansion analysis.

In order to identify the region of good designs within the five-dimensional design space, we use an in-house search optimizer with random restarts to collect a small set of six devices that all have CEs above 73% and are separated by 20 nm in Manhattan distance (MD $= \sum_i |L_i^{(1)} - L_i^{(2)}|$). We then apply a dimensionality reduction strategy on these six design points using linear principal component analysis (PCA) and find that two effective design parameters (i.e. principal components) are sufficient [10] to represent the subspace of good designs. In other words, the subspace in which all of the high performance designs reside can be well approximated as a 2D hyperplane, $\mathrm{X} = \alpha \mathrm{V}_1 + \beta \mathrm{V}_2 + \mathrm{C}$ with $\mathrm{V}_1 = [17.1\,\mathrm{nm}, 1.4\,\mathrm{nm}, 29.0\,\mathrm{nm}, -33.1\,\mathrm{nm}, -0.04]$, $\mathrm{V}_2 = [-1.3\,\mathrm{nm}, -19.8\,\mathrm{nm}, 17.0\,\mathrm{nm}, -9.1\,\mathrm{nm}, 0.07]$, and $\mathrm{C} = [268\,\mathrm{nm}, 69\,\mathrm{nm}, 233\,\mathrm{nm}, 123\,\mathrm{nm}, 2.57]$. Therefore, a good design point X in the original five-dimensional space can be described using only two parameters $\alpha$ and $\beta$. Through projecting the set of six designs onto the 2D hyperplane, we verify a small average projection error of 12 nm in Manhattan distance $\sum_i |L_i^{(projected)} - L_i^{(original)}|$, that is on average 3 nm per segment (well within the fabrication errors), and an average of 0.02 in index difference $|n_{\mathrm{swg}}^{projected} - n_{\mathrm{swg}}^{original}|$. This projection also induces an average estimation error of 3% for the CE. Reducing the number of design parameters from 5 to 2 enables the identification of new designs through rapid and exhaustive mapping of the subspace, not only for the primary optimization objective

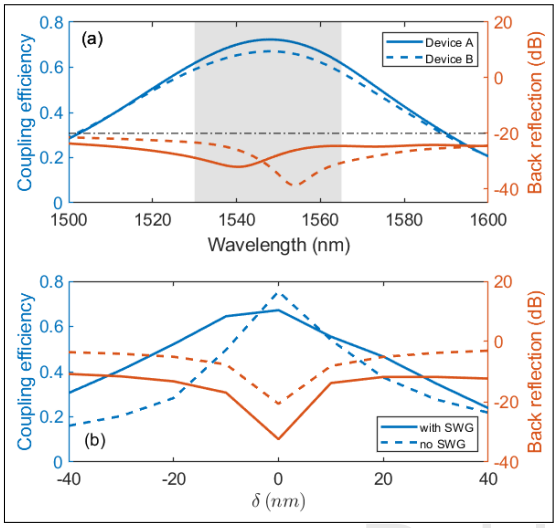


**Fig. 3.** (a) Vertical coupling efficiency and back reflection computed with 3D-FDTD for broadband device A (mFS=106 nm, $\Lambda_{swg} = 450$ and $DC_{swg} = 0.71$) and device B (mFS=130 nm, $\Lambda_{swg} = 450$ and $DC_{swg} = 0.67$) of Fig. 2. (b) Same quantities at $\lambda = 1550$ nm for the SWG device B compared to a non-SWG five-segment design [7, 10] with $L = [77, 84, 115, 249, 171]$ nm, where $\delta$ is the change of the SWG/pillar segment size.

but also for other figures-of-merit. The resulting performance maps are presented in Fig. 2 for both CE and BR and the original six devices used to perform the dimensionality reduction are marked with dots. These maps reveal the global optimum for CE and BR. They furthermore shed light on regions that were originally unknown or only partially revealed. For example, there is only one design in the original set of six with an mFS larger than 100 nm. Upon mapping, Fig. 2 shows that a large portion of the design subspace includes devices with mFS $\geq 100$ nm and even $\geq 130$ nm, enclosed by the dashed and solid lines, respectively. It is of interest to note that the boundaries of these regions are set by different design features. In particular, the two straight sides are enforced by the mFS specification (reached by L2 for the longer side and L4 for the shorter side) whereas the third curved boundary is set by the minimum CE of 60%. Note that, within the larger enclosed area, coupling efficiencies are as high as 75% near $[\alpha, \beta] = [1.0, -1.5]$.

From the design maps created using 2D simulations, we select a number of designs according to the desired mFS, and then further optimize them using 3D-FDTD simulations by scanning the SWG duty cycle. Our goal is achieving broadband low BR and high CE. To proceed with 3D simulations, the non-SWG segments are simply extended in the transverse direction to 15 µm which is also the width of the input slab waveguide. To construct the SWG segment, the silicon layer is periodically patterned in the transverse direction using an SWG period $\Lambda_{swg} = 450$ nm and a duty cycle $DC_{swg} = a/\Lambda_{swg}$. We find that the devices labeled as A and B in Fig. 2 with mFS of 106 nm ($X_A = [272\,\text{nm}, 106\,\text{nm}, 204\,\text{nm}, 138\,\text{nm}, 2.42]$) and 130 nm ($X_B = [280\,\text{nm}, 130\,\text{nm}, 196\,\text{nm}, 134\,\text{nm}, 2.32]$), respectively, exhibit broadband low back-reflections of below -20 dB over more than 100 nm bandwidth, and have high CEs at the center wavelength of 1550 nm. The corresponding spectral response are presented in Fig. 3, with $DC_{swg} = 0.71$ for device A and DC-swg=0.6 for device B, ensuring feature sizes larger than 100 nm and 130 nm in the transverse direction. Device A shows a maximum coupling efficiencies of 72% at $\lambda = 1550$ nm with a 1-dB bandwidth of 43 nm, while device B correspondingly shows a CE = 67% with a 1-dB bandwidth of 45 nm. These bandwidths in CE are similar to those obtained with non-SWG gratings which have smaller feature sizes [7, 10]. As expected, the device with the smaller feature size provides a slightly higher CE. Nonetheless, with the new geometry proposed here, devices with all feature sizes above the 130 nm mark still offer respectable performance.

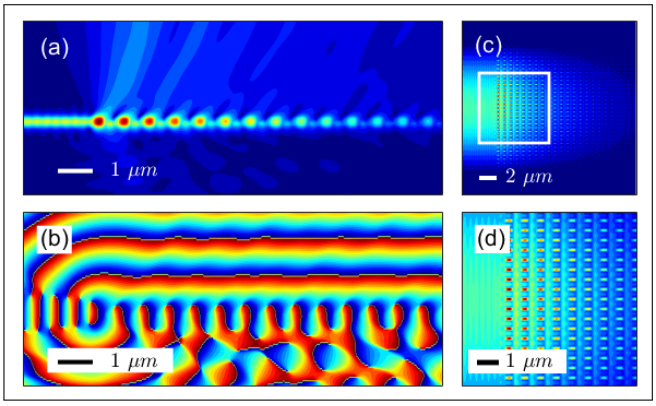


**Fig. 4.** 3D-FDTD simulated scattered field for the device A. (a)-(b) show the side-view of the magnitude and the phase for the field diffracted away from the grating, respectively. (c)-(d) show the top-view at 55 nm above the box (half-way through the shallow etched segment). (d) is a zoom-in of the field plotted in (c), highlighted by the white rectangle.

To further reveal the importance of the SWG segment, we study the impact of its dimension variations on the device performance. We vary the segment size by $\delta$ such that $L_1 = L_1 + \delta$, $L_2 = L_2 - \delta$, $a = a + \delta$ and plot the CE and BR at 1550 nm in Fig. 3 (b). For comparison, we repeat a similar analysis for a previously reported non-SWG five-segment design [10], on its pillar segment that was shown to suppress the BR [7]. As seen, the SWG-based grating leads to smaller changes for CE and maintains a lower level of BR for $\pm 40$ nm dimension variations. This is likely due to the relatively larger size and lower refractive index of the SWG segment.

In Fig. 4, we plot (a) the magnitude and (b) the phase of the diffracted E-field of the optimized grating coupler A (same was done for device B) at 1550 nm. The phase plot shows a flat wave-front of the diffracted field that is perfectly parallel to the grating surface, confirming its vertical operation. In terms of the in-plane propagation, both the intensity and phase show neither significant reflections from the grating nor considerable residual power transmitted through the grating. In Fig. 4 (c), we plot the top-view of the scattered E-field where the decay along the grating periodicity is seen. For more details, an expanded view is re-plotted in Fig. 4 (d). Here, one can distinguish the field propagation through the silicon within the SWG segments and strong field amplitudes within the etched regions.

To investigate the robustness of our optimized devices, we perform three sets of studies that represent commonly encountered fabrication variations: (a) varying grating segment sizes that could result from limited fidelity of the lithography or over/under etching; (b) displacing the L-shaped wall between $L_3$ and $L_4$ due to misalignment between the two etch steps; (c) varying the etch depth. We focus on device B with 130 nm mFS.

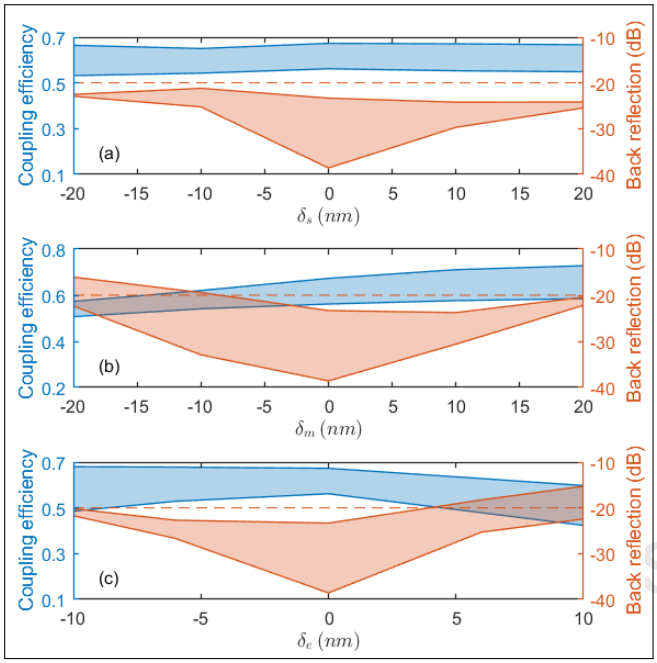


**Fig. 5.** (a) The minimum and maximum (upper and lower bounds of the shaded areas) coupling efficiency and back reflection across the C-band for different values of the segment width variation for device B. Same quantities are plotted for misalignment between the two etch steps in (b) and for the shallow etch variations in (c).

For these simulations, both the diffraction period and the SWG period ($\Lambda = 740$ nm and $\Lambda_{\text{swg}} = 450$ nm) are assumed unaltered during fabrication. In the first study shown in Fig. 5 (a), we plot the minimum and the maximum of BR and vertical CE over the entire C-band for segment size variation $\delta_s$ such that $L_1' = L_1$, $L_2' = L_2 + \delta_s$, $L_3' = L_3$, $L_4' = L_4 - \delta_s$, $a' = a - \delta_s$; note that the two faces for the $L_1$ and $L_3$ are subjected to the same changes and therefore remains unchanged. As seen, over a variation of $\pm 20$ nm the CE changes are small and the BR stay below -20 dB (the low BR extends over more than 100 nm bandwidth in all of these cases). In Fig. 5 (b), we repeat the same analysis for different misalignment values $\delta_m$ such that $L_3' = L_3 + \delta_m$, $L_4' = L_4 - \delta_m$. Here, because the misalignment modifies the aspect ratio of the L-shaped segment, the impact on power diffracted upwards and therefore the CE is more pronounced; however, the BR still stays below the -20 dB mark over a wide range. Note that, for positive values of $\delta_m$ higher CE values are obtained, but these devices have feature sizes smaller than 130 nm. Finally, in Fig. 5 (c), we show an additional analysis where variations of the shallow etch step are considered, i.e. $h_{\text{shallow}} = h_{\text{shallow}} + \delta_e$. Such deviations are expected to be within $\pm 10$ nm [19] and according to Fig. 5 (c), some degradation of the CE is expected while the back BR mostly remains below -20 dB. Therefore, subjected to fabrication variations, the BR profile for the proposed SWG-based grating couplers is quite robust.

In conclusion, we have presented a perfectly vertical grating coupler geometry that is compatible with 193 nm DUV dry lithography in terms of the mFS. The couplers are based on a 220 nm SOI platform using the standard two-step etch process. By applying dimensionality reduction using PCA, we discover a subspace of good designs that can be characterized using a 2D hyperplane. Full exploration of this hyperplane with regard to the coupling efficiency, back reflection and minimum feature size provides the knowledge for making informed trade-offs. The map reveals a design area that maintains a high CE of up to 75% with a mFS of $\geq$ 100 nm. Further increase in the mFS to 130 nm causes a small decrease of CE to 67%, verified using 3D-FDTD simulations. We show that selected gratings have very low BRs below -20 dB over more than 100 nm bandwidth and are also very robust against fabrication variations. Indeed, in contrast to non-SWG geometries, our designs maintain these low levels of BR even when subjected to typical fabrication variations including segment size, misalignment and etch depth. Our perfectly vertical grating geometry paves the way toward efficient and fabrication-tolerant interfacing between fiber arrays and integrated chips that can be mass-produced.

**Disclosures.** The authors declare no conflicts of interest.

## REFERENCES


1. R. Halir, P. Cheben, S. Janz, D.-X. Xu, I. Molina-Fernández, and J. G. Wangüemert-Pérez, Opt. Lett. **34**, 1408 (2009).
2. R. Halir, P. Cheben, J. H. Schmid, R. Ma, D. Bedard, S. Janz, D.-X. Xu, A. Densmore, J. Lapointe, and I. Molina-Fernández, Opt. Lett. **35**, 3243 (2010).
3. M. Antelius, K. B. Gylfason, and H. Sohlström, Opt. Express **19**, 3592 (2011).
4. D. Benedikovic, C. Alonso-Ramos, P. Cheben, J. H. Schmid, S. Wang, D.-X. Xu, J. Lapointe, S. Janz, R. Halir, A. Ortega-Moñux, J. G. Wangüemert-Pérez, I. Molina-Fernández, J.-M. Fédéli, L. Vivien, and M. Dado, Opt. Lett. **40**, 4190 (2015).
5. A. Bozzola, L. Carroll, D. Gerace, I. Cristiani, and L. C. Andreani, Opt. Express **23**, 16289 (2015).
6. D. Benedikovic, C. Alonso-Ramos, D. Pérez-Galacho, S. Guerber, V. Vakarin, G. Marcaud, X. Le Roux, E. Cassan, D. Marris-Morini, P. Cheben, F. Boeuf, C. Baudot, and L. Vivien, Opt. Lett. **42**, 3439 (2017).
7. T. Watanabe, M. Ayata, U. Koch, Y. Fedoryshyn, and J. Leuthold, J. Light. Technol. **35**, 4663 (2017).
8. N. V. Sapra, D. Vercruysse, L. Su, K. Y. Yang, J. Skarda, A. Y. Piggott, and J. Vučković, arXiv:1808.07630 [physics] (2018). ArXiv: 1808.07630.
9. A. Michaels and E. Yablonovitch, Opt. Express **26**, 4766 (2018).
10. D. Melati, Y. Grinberg, M. Kamandar Dezfouli, S. Janz, P. Cheben, J. H. Schmid, A. Sánchez-Postigo, and D.-X. Xu, Nat. Commun. **10**, 4775 (2019).
11. L. Su, R. Trivedi, N. V. Sapra, A. Y. Piggott, D. Vercruysse, and J. Vučković, Opt. Express **26**, 4023 (2018).
12. "ePIXfab-European Silicon Photonics Alliance – European Silicon Photonics Alliance," .
13. Y. Tong, W. Zhou, and H. K. Tsang, Opt. Lett. **43**, 5709 (2018).
14. P. Cheben, R. Halir, J. H. Schmid, H. A. Atwater, and D. R. Smith, Nature. **560**, 565 (2018).
15. R. Halir, P. J. Bock, P. Cheben, A. Ortega-Moñux, C. Alonso-Ramos, J. H. Schmid, J. Lapointe, D.-X. Xu, J. G. Wangüemert-Pérez, I. Molina-Fernández, and S. Janz, Laser & Photonics Rev. **9**, 25 (2015).
16. J. Parra and P. Sanchis, "Particle swarm optimization for polarization-independent and low loss grating couplers," in *2017 Joint Session ECIO / OWTNM W3,* (2017).
17. P. J. Bock, P. Cheben, J. H. Schmid, J. Lapointe, A. Delâge, S. Janz, G. C. Aers, D.-X. Xu, A. Densmore, and T. J. Hall, Opt. Express **18**, 20251 (2010).
18. Z. Cheng, X. Chen, C. Y. Wong, K. Xu, and H. K. Tsang, Appl. Phys. Lett. **101**, 101104 (2012).
19. D.-X. Xu, J. H. Schmid, G. T. Reed, G. Z. Mashanovich, D. J. Thomson, M. Nedeljkovic, X. Chen, D. V. Thourhout, S. Keyvaninia, and S. K. Selvaraja, IEEE J. Sel. Top. Quantum Electron. **20**, 189 (2014).

## FULL REFERENCES


1. R. Halir, P. Cheben, S. Janz, D.-X. Xu, I. Molina-Fernández, and J. G. Wangüemert-Pérez, "Waveguide grating coupler with subwavelength microstructures," Opt. Lett. **34**, 1408 (2009).
2. R. Halir, P. Cheben, J. H. Schmid, R. Ma, D. Bedard, S. Janz, D.-X. Xu, A. Densmore, J. Lapointe, and I. Molina-Fernández, "Continuously apodized fiber-to-chip surface grating coupler with refractive index engineered subwavelength structure," Opt. Lett. **35**, 3243 (2010).
3. M. Antelius, K. B. Gylfason, and H. Sohlström, "An apodized SOI waveguide-to-fiber surface grating coupler for single lithography silicon photonics," Opt. Express **19**, 3592 (2011).
4. D. Benedikovic, C. Alonso-Ramos, P. Cheben, J. H. Schmid, S. Wang, D.-X. Xu, J. Lapointe, S. Janz, R. Halir, A. Ortega-Moñux, J. G. Wangüemert-Pérez, I. Molina-Fernández, J.-M. Fédéli, L. Vivien, and M. Dado, "High-directionality fiber-chip grating coupler with interleaved trenches and subwavelength index-matching structure," Opt. Lett. **40**, 4190 (2015).
5. A. Bozzola, L. Carroll, D. Gerace, I. Cristiani, and L. C. Andreani, "Optimising apodized grating couplers in a pure SOI platform to -0.5 dB coupling efficiency," Opt. Express **23**, 16289–16304 (2015).
6. D. Benedikovic, C. Alonso-Ramos, D. Pérez-Galacho, S. Guerber, V. Vakarin, G. Marcaud, X. Le Roux, E. Cassan, D. Marris-Morini, P. Cheben, F. Boeuf, C. Baudot, and L. Vivien, "L-shaped fiber-chip grating couplers with high directionality and low reflectivity fabricated with deep-UV lithography," Opt. Lett. **42**, 3439 (2017).
7. T. Watanabe, M. Ayata, U. Koch, Y. Fedoryshyn, and J. Leuthold, "Perpendicular Grating Coupler Based on a Blazed Antiback-Reflection Structure," J. Light. Technol. **35**, 4663–4669 (2017).
8. N. V. Sapra, D. Vercruysse, L. Su, K. Y. Yang, J. Skarda, A. Y. Piggott, and J. Vučković, "Inverse design and demonstration of broadband grating couplers," arXiv:1808.07630 [physics] (2018). ArXiv: 1808.07630.
9. A. Michaels and E. Yablonovitch, "Inverse design of near unity efficiency perfectly vertical grating couplers," Opt. Express **26**, 4766 (2018).
10. D. Melati, Y. Grinberg, M. Kamandar Dezfouli, S. Janz, P. Cheben, J. H. Schmid, A. Sánchez-Postigo, and D.-X. Xu, "Mapping the global design space of nanophotonic components using machine learning pattern recognition," Nat. Commun. **10**, 4775 (2019).
11. L. Su, R. Trivedi, N. V. Sapra, A. Y. Piggott, D. Vercruysse, and J. Vučković, "Fully-automated optimization of grating couplers," Opt. Express **26**, 4023–4034 (2018).
12. "ePIXfab-European Silicon Photonics Alliance – European Silicon Photonics Alliance," .
13. Y. Tong, W. Zhou, and H. K. Tsang, "Efficient perfectly vertical grating coupler for multi-core fibers fabricated with 193 nm DUV lithography," Opt. Lett. **43**, 5709 (2018).
14. P. Cheben, R. Halir, J. H. Schmid, H. A. Atwater, and D. R. Smith, "Subwavelength integrated photonics," Nature. **560**, 565 (2018).
15. R. Halir, P. J. Bock, P. Cheben, A. Ortega-Moñux, C. Alonso-Ramos, J. H. Schmid, J. Lapointe, D.-X. Xu, J. G. Wangüemert-Pérez, I. Molina-Fernández, and S. Janz, "Waveguide sub-wavelength structures: a review of principles and applications: Waveguide sub-wavelength structures," Laser & Photonics Rev. **9**, 25–49 (2015).
16. J. Parra and P. Sanchis, "Particle swarm optimization for polarization-independent and low loss grating couplers," in *2017 Joint Session ECIO / OWTNM W3,* (2017).
17. P. J. Bock, P. Cheben, J. H. Schmid, J. Lapointe, A. Delâge, S. Janz, G. C. Aers, D.-X. Xu, A. Densmore, and T. J. Hall, "Subwavelength grating periodic structures in silicon-on-insulator: a new type of microphotonic waveguide," Opt. Express **18**, 20251–20262 (2010).
18. Z. Cheng, X. Chen, C. Y. Wong, K. Xu, and H. K. Tsang, "Apodized focusing subwavelength grating couplers for suspended membrane waveguides," Appl. Phys. Lett. **101**, 101104 (2012).
19. D.-X. Xu, J. H. Schmid, G. T. Reed, G. Z. Mashanovich, D. J. Thomson, M. Nedeljkovic, X. Chen, D. V. Thourhout, S. Keyvaninia, and S. K. Selvaraja, "Silicon Photonic Integration Platform—Have We Found the Sweet Spot?" IEEE J. Sel. Top. Quantum Electron. **20**, 189–205 (2014).